Physical Properties of the Lyman Alpha Forest in a Cold Dark Matter Cosmology

Yu Zhang[1,2], Avery Meiksin[3,4], Peter Anninos[1], and Michael L. Norman[1,2]

[1] *Laboratory for Computational Astrophysics, National Center for Supercomputing Applications, University of Illinois at Urbana-Champaign, 405 N. Mathews Ave., Urbana, IL 61801*

[2] *Astronomy Department, University of Illinois at Urbana- Champaign, 1002 West Green Street, Urbana, IL 61801*

[3] *Department of Astronomy & Astrophysics, University of Chicago, 5640 South Ellis Avenue, Chicago, IL 60637*

[4] *Edwin P. Hubble Research Scientist*

ABSTRACT

We discuss the origin and physical nature of the Lyα forest absorption systems as found in hydrodynamical simulations of the Intergalactic Medium (IGM) in a standard Cold Dark Matter cosmology ($\Omega = 1$, $H_0 = 50\,\mathrm{km\,s^{-1}\,Mpc^{-1}}$, $\sigma_8 = 0.7$). The structures of the systems that give rise to the Lyα forest span a wide range in morphologies, depending on the density contrast. Highly overdense systems, $\rho_b/\bar{\rho}_b \gtrsim 10$, where ρ_b denotes baryon density, tend to be spheroidal and are located at the intersections of an interconnecting network of filaments of moderate overdensity, $1 \lesssim \rho_b/\bar{\rho}_b \lesssim 5$. The typical thickness of the filaments is 100 kpc, with a typical length of a few megaparsecs. At the cosmological average density, the characteristic morphology is cell–like with underdense regions separated by overdense sheet–like partitions. The lowest density contours tend to enclose amorphous, isolated regions. We find that the principal structures of the IGM are in place by $z = 5$, with the evolution in the IGM absorption properties due primarily to the expansion of the universe and the changing intensity of the photoionizing background radiation field. The absorption properties of the forest clouds correlate strongly with those of the underlying physical systems from which they arise. The highest column density systems ($\log N_{\mathrm{HI}} \gtrsim 15$), correspond to the highly overdense spheroidal structures, moderate column density systems ($13 \lesssim \log N_{\mathrm{HI}} \lesssim 14$), correspond to the filaments, and the lowest density absorption systems originate from discrete fluctuations within underdense regions a few megaparsecs across, cosmic minivoids. Most of the intergalactic He II opacity arises from these underdense regions. Similar correlations are found for the cloud temperature and divergence of the peculiar velocity field. Within the uncertainties of the statistics of the derived Lyα forest properties, we are able to account for the distribution of optical depths in our synthesized spectra entirely

by absorption due to discrete systems. We find that virtually all the baryons in the simulation fragment into structures that we can identify with discrete absorption lines, with at most 5% remaining in a smoothly distributed component (the Gunn–Peterson effect). We compare our results with the cloud ionization parameters inferred from Keck HIRES measurements of carbon and silicon in the Lyα forest. Combining with constraints imposed by measurements of the mean intergalactic H I opacity permits separate limits to be set on the mean cosmological baryon density Ω_b and H I ionization rate $\Gamma_{\rm HI}$. For the cosmological model investigated, we find $0.03 \lesssim \Omega_b \lesssim 0.08$ and $0.3 \lesssim \Gamma_{\rm HI,-12} \lesssim 1$ ($\Gamma_{\rm HI,-12} = \Gamma_{\rm HI}/10^{-12}\,{\rm s}^{-1}$), at $z = 3 - 3.5$. Our results for the amount of intergalactic H I and He II absorption and for the ionization parameters of the clouds are consistent with a forest photoionized by a UV background dominated by QSO sources with an intrinsic spectral index of $\alpha_Q \approx 1.8 - 2$.

Subject headings: cosmology: theory – dark matter – intergalactic medium; methods: numerical; quasars: absorption lines

1. Introduction

The last few years have witnessed considerable advances in our understanding of the structure of the Intergalactic Medium (IGM) predicted by Cold Dark Matter (CDM) dominated cosmologies. Several groups have performed a series of combined numerical N-body/ hydrodynamics simulations of structure formation in the IGM (Cen et al. 1994; Zhang, Anninos, & Norman 1995; Hernquist et al. 1996), that are converging on a definite picture for the origin of the Lyα forest in a CDM universe. Although some differences between the simulations remain to be resolved, the general landscape the simulations have drawn is one of an interconnected network of sheets and filaments, with dwarfish spheroidal systems, essentially minihalos (Rees 1986; Ikeuchi 1986), located at their points of intersection, and fluctuations within low density regions between. The filamentary structure bears a remarkable resemblance to the findings of similar simulations for the formation of rich clusters of galaxies (Bryan et al. 1994). Bond, Kofman, & Pogosyan (1996) have argued that this "cosmic web" is a generic feature of CDM, a consequence of an inchoate pattern in the matter fluctuations imprinted at the epoch of matter–radiation decoupling and sharpened by gravitational instability. The distribution in neutral hydrogen column densities along lines–of–sight piercing the filaments, as well as the distribution of the velocity widths of the resulting absorption features, are found to coincide closely with the measurements of the Lyα forest in the spectra of high redshift quasars (Miralda-Escudé et al. 1996; Davé et al. 1997; Zhang et al. 1997; Wadsley & Bond 1997).

Ever since the pioneering survey of Sargent et al. (1980), observational studies of the Lyα forest have targeted several key issues concerning the structure of the absorbers: 1. What is the physical state of the clouds? 2. What is the confinement mechanism of the clouds? 3. How do the clouds evolve? 4. What are their shapes and physical extent? 5. How do the clouds fit into scenarios for the formation of large–scale structure? Following the identification of the Lyα absorption lines in QSO spectra as intergalactic H I clouds by Lynds (1971), Arons (1972) attributed the absorption to the hydrogen in intervening protogalaxies photoionized by a QSO–dominated UV background. The essential confinement mechanism in this scenario is the gravity of the protogalaxy. Sargent et al. (1980) suggested an alternative model in which the absorption arises from intergalactic gas clouds confined by a hot ambient IGM. Following their lead, Ostriker & Ikeuchi (1983) and Ikeuchi & Ostriker (1986) formulated a theory of pressure confined clouds that permitted definite predictions to be made for the observed properties of the absorbers and their evolution and for the properties of the hot confining medium. Shortly thereafter, the successes of the CDM model created an interest in combining this theory of large scale structure formation with the formation of Lyα clouds into a single unified picture. In this scenario, Lyα clouds can either be associated with bound structures, stabilized by the gravity of dark matter mini–halos (Rees 1986, 1988; Ikeuchi 1986), or with post–photoionized unconfined gas in low mass objects that developed from small mass fluctuations (Bond, Szalay, and Silk 1988). Subsequent discussions of the structure and evolution of the clouds included a link to dwarf galaxy formation (Ikeuchi & Norman 1987; Ikeuchi, Murakami, & Rees 1988), the effect of environment on minihalos (Murakami & Ikeuchi 1994), and slab models for the clouds (McGill 1990; Charlton, Salpeter, & Hogan 1993; Miralda–Escudé & Rees 1993; Meiksin 1994).

Parallel to the investigations of the Lyα forest has been a closely allied effort to study the structure of a smoothly distributed diffuse intergalactic gas component. Soon after the identification of the first QSO, Gunn & Peterson (1965) recognized that its spectrum could be used to place a stringent constraint on the number density of neutral hydrogen in the IGM by measuring the amount of Lyα absorption shortward of the Lyα emission line of the QSO. The absence of a strong absorption trough led them to conclude that the neutral hydrogen density of the IGM is so low that the IGM must be highly ionized. The detection of such a component would have important consequences for cosmology. Since a lower limit to the amount of metagalactic ionizing radiation is provided by the contribution due to QSO sources, a measurement of the Lyα opacity of a smooth component could be used to determine a lower bound to the total hydrogen density of the IGM, assuming the IGM is in photoionization equilibrium. This density would be directly comparable to the prediction of Big Bang nucleosynthesis. In order to estimate the opacity of the smooth component, however, it is crucial first to remove the contribution to the absorption due to the Lyα forest (Steidel & Sargent 1987; Jenkins & Ostriker 1991). The total density of the diffuse gas may be derived only if its filling factor is known, which, following Gunn & Peterson (1965), was implicitly assumed to be unity. For a clumped component like the forest, the filling factor is not directly amenable to measurements. To date there has been no definitive detection of a smoothly distributed component of neutral hydrogen. Measurements have been made of the amount of absorption by intergalactic He II (Jakobsen et al. 1994; Davidsen et al. 1996; Hogan et al. 1997), but again it appears possible to account for the absorption entirely by the Lyα forest (Madau & Meiksin 1994; Songaila, Hu, & Cowie 1995; Giroux, Fardal, & Shull 1995).

In this paper, we address these questions using the results of our recent numerical hydrodynamics simulations of the formation of the Lyα forest in standard CDM (SCDM). In a companion paper, Zhang et al. (1997), we presented an analysis of synthetic spectra constructed from the simulation results. There we found excellent agreement between the model H I column density distribution over the range $10^{12} < N_{\rm HI} < 10^{16}\,{\rm cm}^{-2}$ and the observed spectra from the Keck HIRES and from previous high spectral resolution studies. We also showed the underlying distribution of Doppler parameters agrees closely with the distribution inferred from observations. We found that agreement with measurements of the intergalactic He II absorption required a fairly soft UV background, but one still compatible with QSOs as the dominant radiation sources. In this paper, we concentrate on the physical structure of the clouds. We make some comparisons with the results from alternative schemes for solving the hydrodynamics. The calculations of Hernquist et al. (1996), Haehnelt et al. (1996), and Wadsley & Bond (1997) were performed using Smoothed Particle Hydrodynamics (SPH), in contrast to the more traditional grid–based code we have adopted. Cen et al. (1994) performed a ΛCDM simulation using a grid–based code, though with a different treatment of the hydrodynamics based on a total variation dimininishing scheme (TVD). We also provide a detailed discussion of a topic that has not received much previous attention, the structure within small underdense regions, minivoids. We shall argue that an understanding of the fine–structure of the minivoids is essential for interpreting measurements of the opacity of the IGM, both of hydrogen and especially of singly ionized helium.

In §2 we briefly describe our numerical method and simulations. In §3 we describe the physical properties of the absorption systems, and relate these to their absorption properties. We discuss the origin of the absorption in the underdense regions in §4 and its observational consequences. We summarize our results in §5.

2. The Simulations

The simulations were performed using our 2–level hierarchical grid code HERCULES (Anninos, Norman, & Clarke 1994; Anninos et al. 1997). The simulation box had a comoving side of 9.6 Mpc. Most of the analysis presented here is for the top grid. To explore the effects of grid resolution, we take advantage of the 2–level nature of our code and introduce a second, more finely resolved, subgrid to cover a section of the coarser top grid. We use 128^3 cells on both the top and subgrids, and 128^3 particles to represent the dark matter. The subgrid is centered on the *least* dense region of the top grid for the purpose of resolving in greater detail the fine density structure of the voids. The subgrid is a factor of 4 greater in resolution. Thus, the top grid has a comoving resolution of 75 kpc and the subgrid of 18.75 kpc. The dark matter particles have a mass of $2.9 \times 10^7\,\mathrm{M}_\odot$ in the top grid, and $4.6 \times 10^5\,\mathrm{M}_\odot$ in the subgrid.

Our model background spacetime is a flat, cold dark matter dominated universe with the initial density perturbations originating from inflation–inspired adiabatic fluctuations. We assume a Hubble constant $H_0 = 50\,\mathrm{km\,s^{-1}\,Mpc^{-1}}$. The BBKS (Bardeen et al. 1986) transfer function is employed with the standard Harrison–Zel'dovich power spectrum, normalized to $\sigma_{8h^{-1}} = 0.7$, where $h = H_0/100\,\mathrm{km\,s^{-1}\,Mpc^{-1}}$, consistent with the present number density and temperatures of galaxy clusters (White, Efstathiou, & Frenk 1993; Bond & Myers 1996). We adopt $\Omega_b = 0.06$, consistent with Big Bang nucleosynthesis limits (Copi, Schramm, & Turner 1995), and the baryonic fluid is composed of hydrogen and helium in primordial abundance with a hydrogen mass fraction of 76%. We generate the initial particle positions and perturbations using the COSmological initial conditions and MICrowave anisotropy codeS (COSMICS, Bertschinger 1995).

In addition to the usual ingredients of baryonic and dark matter, we also solve the coupled system of non–equilibrium chemical reactions with radiative cooling. The reaction network includes a self–consistent treatment of the following six species: H I , H II , He I , He II , He III and e^-. Details of the chemical model, cooling rates and numerical methods can be found in Abel et al. (1997) and Anninos et al. (1997). We include a uniform UV photoionizing background, adopting the estimate of Haardt & Madau (1996) for a QSO-dominated UV background. We turn on the radiation field at $z = 6$. It is unlikely that the H II regions from QSO sources would have percolated before this time (Meiksin & Madau 1993), though it is possible the IGM was reionized earlier by other sources like an early generation of stars or decaying neutrinos. The evolution of systems sufficiently dense as to be in photoionization thermal equilibrium are not expected to be much affected by the turn on time of the radiation field by $z < 5$, but more rarefied systems may be sensitive to the reionization history (Meiksin 1994). The topic merits further investigation. We do not incorporate

radiative transfer through the gas, as the clouds we are most interested in have column densities $N_{\rm HI} < 10^{16}\,{\rm cm}^{-2}$. Radiative transfer of the H I ionizing radiation becomes significant for column densities a factor of several above this. For He II , radiative transfer is just starting to become important for this column density, so that we may slightly overestimate the temperatures of the higher column density systems, but the dynamics should be essentially unaltered at our resolution. We adopt the fits to the photoionization rates from Haardt & Madau (1996), and the fits to their results for the heating rates presented in Zhang et al. (1997). Since the cloud temperatures are not very sensitive to the assumed heating rate, we note that comparisons of our current results with alternative radiation fields or cosmic baryon densities may be made by simply rescaling the ionization fractions using the ratio of parameters $b_{\rm ion} \equiv \Omega_b^2/\Gamma_{-12}$, where Γ_{-12} is the photoionization rate for the species of interest, in units of $10^{-12}s^{-1}$. This is a valid procedure provided the regions have not undergone significant recombination into neutral hydrogen or neutral or singly ionized helium, in which case the accompanying change in the temperatures of the clouds can have a non–negligible effect on the cloud dynamics and structure.[1]

3. Physical Properties of Absorbers

3.1. Morphologies

The cloud population is characterized by a range of morphologies. The highest column density systems tend to be associated with physically more dense and compact structures, similar to the minihalo model. These spheroidal systems are interconnected by a network of sheets and filaments. It is these structures that are responsible for most of the traditional Lyα forest, with column densities in the range $10^{13} < N_{\rm HI} < 10^{15}\,{\rm cm}^{-2}$. In between the filaments are underdense regions. Even though underdense, these regions give rise to discrete absorption systems as well. Because the underlying physical origin of these systems appears distinct from those above, and because of its relevance to the detection of a smooth diffuse IGM component, we defer a more complete discussion of the systems in the underdense regions until the following section.

Although no unique attribute suffices to describe the full range of morphologies exhibited by the clouds, systems of a given baryon overdensity are associated with distinctive shapes and configurations. In Plate 1, we show the configurations enclosed by 3D isodensity contours at $z = 3$. At low densities (first panel, $\rho/\bar{\rho} = 0.1$), the contours enclose isolated amorphous regions. These lie at the centers of minivoids, underdense regions a few (comoving) megaparsecs across, as shown in the second and third panels ($\rho/\bar{\rho} = 0.3$ and $\rho/\bar{\rho} = 0.5$). The systems corresponding to the cosmological average density ($\rho/\bar{\rho} = 1$), in the fourth panel show a cell–like or spongy morphology,

[1]Because of the temperature dependence of the radiative recombination rates, a slight dependence of the gas temperature on the baryon density reduces the scaling of the ionization fraction to being somewhat weaker than in direct proportion to $b_{\rm ion}$.

with underdense regions separated by wall–like partitions of varying thicknesses. The next panel ($\rho/\bar{\rho} = 3$), shows a filamentary network emerging from the intersections of the walls. The network, or cosmic web, is prominent in the final panel ($\rho/\bar{\rho} = 10$). We have provided an accompanying video that more vividly displays the transitions between the various morphologies and their interrelations.

In Figure 1, we show two dimensional contour plots of the baryons and the dark matter, as well as the baryonic temperature and peculiar velocity divergence, at $z = 3$. Three–dimensional representations of the results from this and an earlier simulation (Zhang et al. 1996), are available at our WWW site http : //zeus.ncsa.uiuc.edu : 8080/LyA/minivoid.html, and in Norman (1996). The plots in Figure 1 show a slice with a width 1/16 of the box size. There are obvious morphological distinctions between the high and low density structures. The high overdense structures (thick solid lines), are typically isolated objects with an elongated or spheroidal baryon distribution. The baryon distribution closely follows the dark matter distribution. Typical thicknesses of the structures are $30-100$ kpc, though the baryons show coherence over scales as great as a megaparsec. Both the baryons and the dark matter show alignments in their isolated structures over megaparsec scales, defining a network of sheets and filaments. The intermediate density absorbers (solid and dashed lines), are associated mainly with the filaments or sheets themselves. The negative peculiar velocity divergence of these systems shows that they are still undergoing gravitational collapse. The lowest density clouds arise in the underdense ($\rho_b/\overline{\rho}_b < 1$), minivoids between the filaments. The underdense absorbers (dotted lines), tend to be irregular in shape and have no preferred direction as in the case of the filaments and sheets. They typically have temperatures lower than the equilibrium temperature of $\sim 10^4$ K and a positive peculiar velocity divergence, indicating that these regions are expanding with respect to the Hubble flow. There is a general correspondence between high (low) overdensities, high (low) temperatures, and large (small) negative peculiar velocity divergences.

The corresponding H I and He II column density contours are shown in Figure 2. A comparison with Figure 1 shows a clear correlation between column density and overdensity. The high column density absorbers ($N_{\rm HI} > 10^{15}\,{\rm cm}^{-2}$ and $N_{\rm HeII} > 10^{17}\,{\rm cm}^{-2}$) correspond to the highly overdense structures ($\rho_b/\overline{\rho}_b > 10$) residing mostly along and at the intersections of filaments. The medium column density absorbers ($\sim 10^{13-14}\,{\rm cm}^{-2}$ for H I and $\sim 10^{15-16}\,{\rm cm}^{-2}$ for He II) correspond to the modestly overdense filaments ($1 < \rho_b/\overline{\rho}_b < 5$). The column density can be coherent over the scale of a few megaparsecs at this level. The lowest column density absorbers ($\sim 10^{12}\,{\rm cm}^{-2}$ for H I and $\sim 10^{14}\,{\rm cm}^{-2}$ for He II) are associated with underdense structures ($\rho_b/\overline{\rho}_b < 1$) and are located in the void regions between the filamentary structures. They are typically a few hundred kiloparsecs across.

An evolutionary sequence is shown in Figure 3 of the baryonic overdensity over the redshift range $z = 5$ to z= 2. Superimposed is the peculiar velocity field projected onto the plane of the slice. As the universe evolves towards the lower redshifts, the average density decreases due to cosmic expansion, yet the structures remain nearly constant in morphology. There is some indication that the filaments sharpen with time, and that the dense regions at the intersections become more dense, but by and large the principal structures are in place by $z = 5$. The simulations show that once

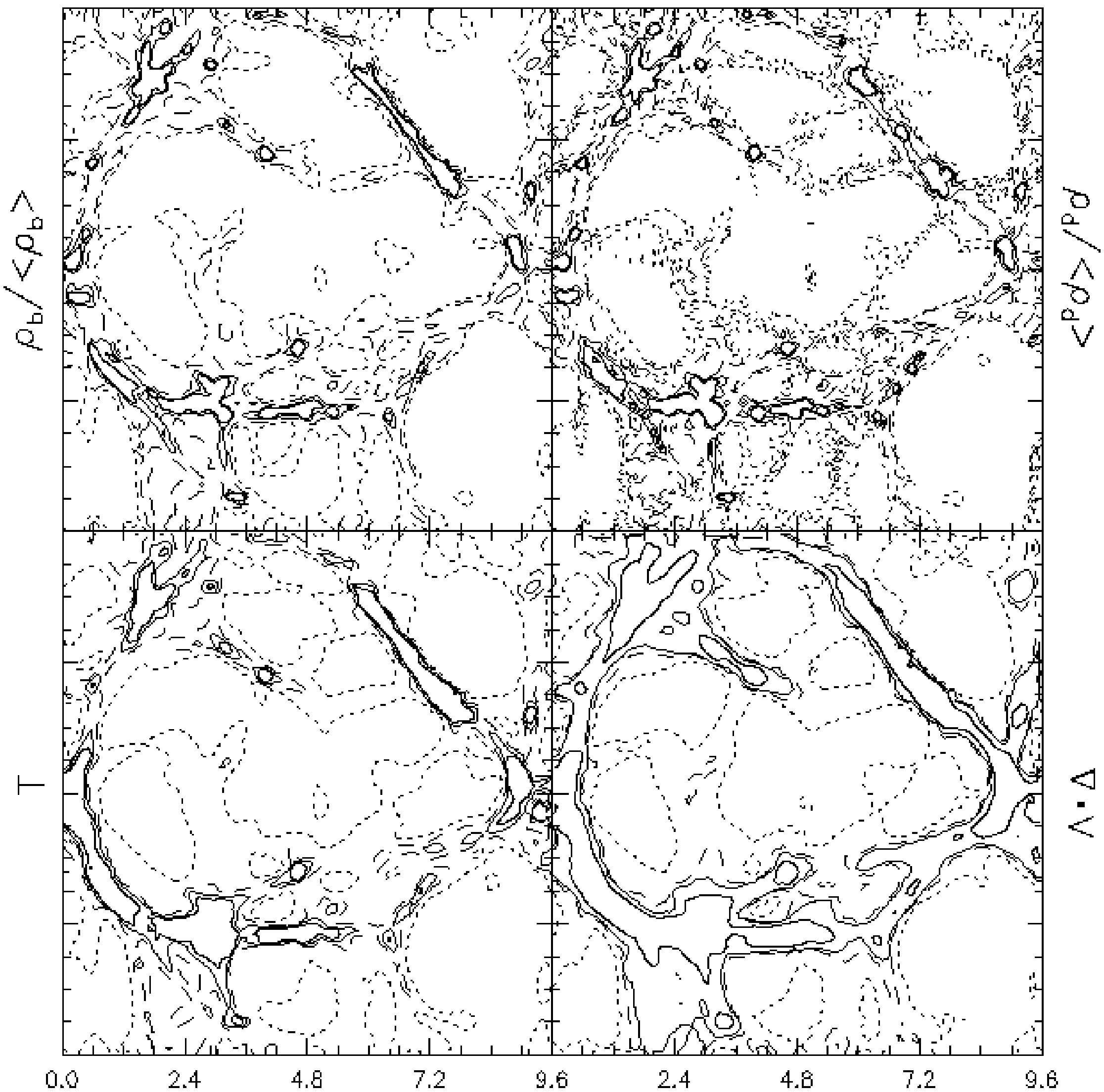

Fig. 1.— Two–dimensional contour plots of the baryon and dark matter overdensity distribution, the temperature, and the divergence of the peculiar velocity field, at $z = 3$. The slice shown has a thickness of 1/16 of the box size, or 150 kpc at $z = 3$. The contour levels for the baryon and dark matter densities are set at: 0.5 (*dotted*), 1 (*dashed*), 3 (*thin solid*), and 5 (*thick solid*). The temperature contour levels, in units of 10^3 K, are: 6 (*dotted*), 10 (*dashed*), 14 (*thin solid*), and 20 (*thick solid*). The peculiar velocity divergence contours, in units of H_0, are: 5 (*dotted*), 0 (*dashed*), -3 (*thin solid*), and -15 (*thick solid*). Overdense regions tend to be associated with warmer gas and a negative peculiar velocity divergence, indicating collapse. By contrast, the underdense regions are expanding, resulting in lower temperatures than given by photoionization thermal equilibrium.

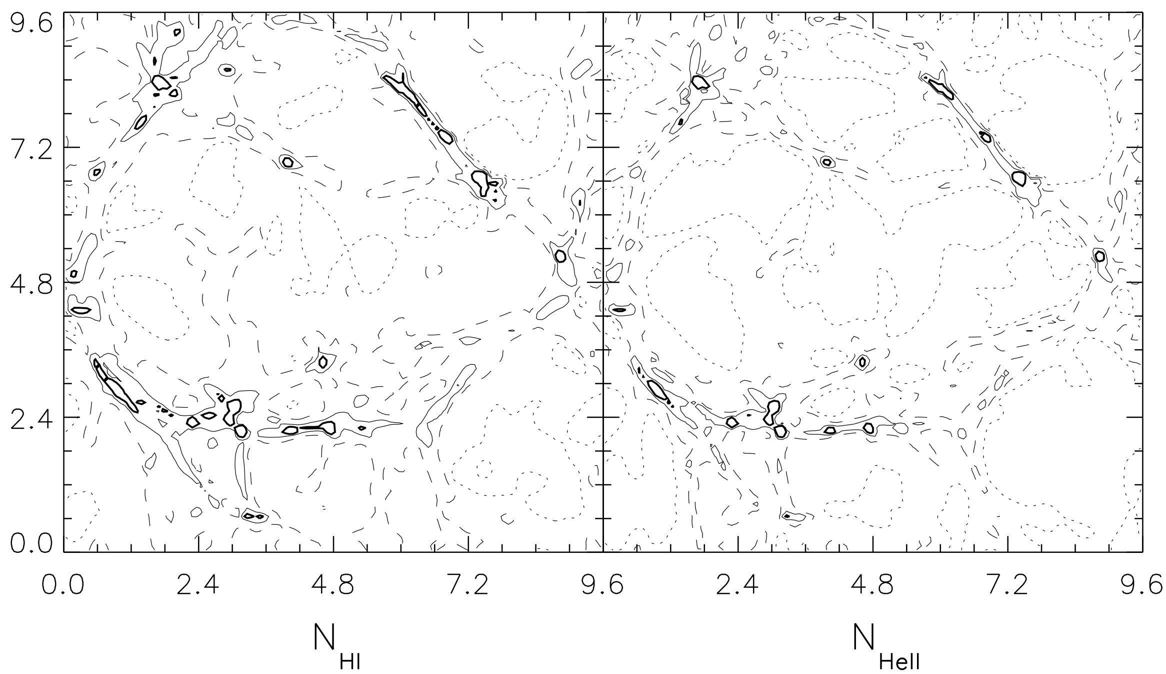

Fig. 2.— Contour plots of the H I and He II column density distributions at $z = 3$, integrated directly through 1/16 of the box size. The contour levels corresponding to the dotted, dashed, thin, and thick solid lines are, respectively, $\log N_{\rm HI} = 12$, 13, 14, and 15, and $\log N_{\rm HeII} = 14$, 15, 16, and 17. The optically thin H I systems ($\log N_{\rm HI} < 13$), are associated with the underdense regions shown in Figure 1. The saturated lines are associated with the filaments and sheets of moderate overdensity. The highest column densities ($\log N_{\rm HI} > 15$) coincide with the largest spheroidal overdense systems at the nodes of intersecting filaments.

Fig. 3.— An evolutionary sequence of the baryon overdensity distribution, shown at $z = 2$, 3, 4, and 5. Superimposed is the peculiar velocity field. A region of spheroidal collapse is visible in the mid left hand portion, while collapse onto an oblique sheet occurs slightly to the right of center. Notice the flow along the elongated structures leading into the pancake, particularly at $z = 3$ and $z = 2$. Only moderate evolution in the overdensity occurs in the sheets and filaments, which themselves are overdense by only a factor of a few. Most of the universe is occupied by underdense regions, with an associated divergent peculiar velocity field.

in place, the sheets and filaments maintain a nearly constant overdensity with time. By contrast, the collapse of a halo is apparent along the lower left side of the plot. The halo is at the center of a strongly convergent velocity flow, and continues to accrete material from the surrounding underdense regions and from along the filaments throughout the simulation. A pancake is visible slightly offset to the right from the center of the figure, at an oblique angle. The continual collapse of material onto the pancake is indicated by the velocity field, which is nearly perpendicular to the pancake surface. Notice the flow along the elongated structures leading into the pancake as well, as is especially clear in the figure at $z = 3$ and $z = 2$. The general pattern is one of outflow from the minivoids, compression into sheets at the boundaries of the voids, and a resulting flow along the sheets toward their intersections. The underdense regions themselves are not uniform, but reveal small–scale mottling and striations. All these structures give rise to discrete absorption features in our synthesized spectra.

The slow evolution of the baryon density is reflected by the distribution of the baryon overdensity, shown in Figure 4. The mode of the distribution shifts to lower values as the underdense regions continue to vacate, resulting in a broadening of the overall distribution. For comparison, we show the evolution of the dark matter overdensity distribution in Figure 5. Theoretical considerations suggest that the density distribution should be approximately lognormal (Coles & Jones 1991; Colombi 1994). We find that a lognormal distribution fits both the baryon and the dark matter overdensity distributions moderately well, as was similarly found for the cell occupation densities in the simulations of Coles, Melott, & Shandarin (1993). Both distributions, however, have pronounced high density tails, so that the probability distribution of the rarer overdense structures is distinctly not lognormal. At low densities, the baryon density distribution cuts off more sharply than a lognormal distribution, while the dark matter distribution shows a broad wing that is also not lognormal.

The constancy of the baryonic overdensity in the sheets is an expected consequence of pancake collapse. The computations of Meiksin (1994) for the collapse of photoionized gas into slabs show that a weak counterflow develops after the formation of a caustic in the dark matter distribution and the subsequent diminishing of the gravitational potential of the slab. This outflow meets the larger inflow in an accretion shock, the position of which moves outward from the slab center. The result is a baryonic density within the slab that decreases nearly in proportion to the cosmic average density. The decrease in baryon density is reflected by a rapid decrease in the H I column density of the slab. In Figure 6, we show the evolution of the column density in the simulation. A consequence of the evolution is that the universe becomes more transparent with time. The number of systems detected along a given line–of–sight above a fixed column density threshold decreases toward decreasing redshift, at a rate consistent with observations (Zhang et al. 1997). The contours, *at the same fixed levels*, become less connected and the sheets and filaments become less extended in space. Despite this general contraction, the *total* number of lines actually increases per unit redshift at lower redshifts as the comoving scale increases for a fixed redshift interval (Zhang et al. 1997, Figure 12).

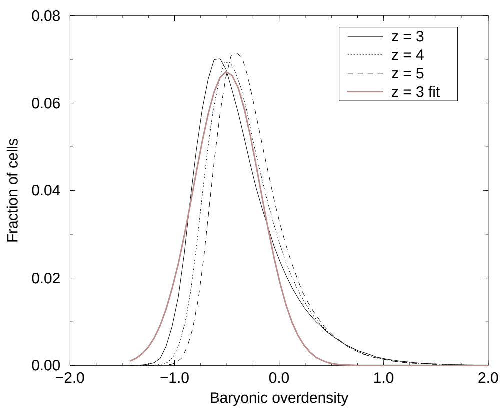

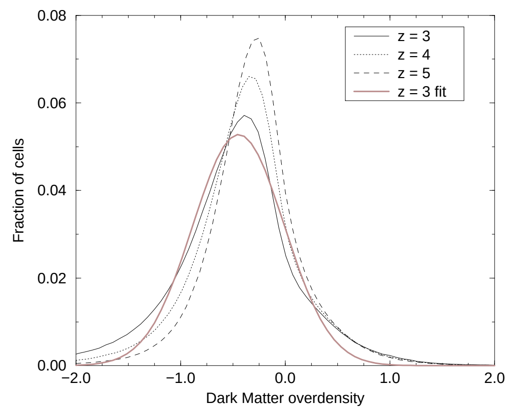

Fig. 4.— The distribution of baryon overdensity, at $z = 3$, 4, and 5. Consistent with the slow evolution in Figure 3, the distributions are nearly identical, with a drift of the mode toward lower values as the underdense regions continue to vacate. The long tail toward higher overdensities accounts for the higher column density H I systems. Also shown is the best fit to a lognormal distribution at $z = 3$.

Fig. 5.— The distribution of the dark matter overdensity, at $z = 3$, 4, and 5. Most of the distribution is well–fit by a lognormal distribution, although tails in the distribution occur at the low and high density extremes. Also shown is the best fit to a lognormal distribution at $z = 3$.

Fig. 6.— An evolutionary sequence of the H I column density, at $z = 2$, 3, 4, and 5. In contrast to the baryonic overdensity, the H I column density levels break up with time, and the universe becomes more transparent as it evolves.

3.2. Physical State of the Clouds

3.2.1. Correlations with HI Column Density

A strong correlation exists not only between baryon density and H I column density, but between temperature, peculiar velocity divergence, and the ratio of dark matter to baryonic overdensities as well. In Figure 7 we show scatter plots of these quantities, along with the average and median dependences on $N_{\rm HI}$. (Also see Zhang et al. 1997; Meiksin 1997). Similar correlations were found for a ΛCDM model (Miralda-Escudé et al. 1996). The temperature of the baryons varies over the range of about 5000 K in expanding regions to over 10^6 K in strongly collapsing regions. Most of the gas mass is in photoionization thermal equilibrium with the ionizing background, and so has a characteristic temperature of $15 - 30 \times 10^3$ K , as shown in Figure 1. In Figure 8a we show a line plot across the densest structure on the top grid of the 9.6 Mpc simulation at redshift $z = 3$. The temperature in most of the cells is elevated to about $1\,{\rm eV}$ due to photoionization heating by the UV radiation background. The densest structures on the grid have a typical caustic–like shape, i.e. the outskirts of the collapsing gas are shock–heated to more than $100\,{\rm eV}$ due to the infalling gas, while the center of the structure is radiatively–cooled (mostly by hydrogen line cooling) to the hydrogen recombination determined temperature of $\sim 1\,{\rm eV}$. Similar structures were found in the simulations of Cen et al. (1994). The gas is completely ionized except in the center–most regions of the densest structures. Typical fractional abundances of H I and He II are roughly 10^{-6} and 10^{-4} respectively. However, at the centers of the densest structures, hydrogen and helium have mostly recombined to their neutral forms. Figure 8b shows the corresponding line plot across the densest cell in the sub grid simulation. Because the subgrid is positioned over the most *underdense* void region of the top grid, the temperatures of the densest structures found on the subgrid are typically lower than those on the top grid.

The high temperatures ($T \gg 10^4\,{\rm K}$) found are readily explained by gravitational infall. Gas falling into a deep potential well will be shock–heated to the effective virial temperature of the potential well, only to relax to the photoionization equilibrium value downstream. Low temperatures ($T \ll 10^4\,{\rm K}$), however, are also found. These occur in low density regions, where the density of the baryons is too low for the gas to maintain equilibrium at the photoionization temperature against the expansion of the gas. This effect was discussed by Meiksin (1994), where it was shown that when the gas density falls below $n_{\rm H} \simeq 10^{-4}\,{\rm cm}^{-3}$ for $z > 2$ in an otherwise quiescient region, the expansion of the gas will drive it out of photoionization thermal equilibrium, resulting in a temperature below the equilibrium value. The reason is that the rate of energy deposition per baryon by photoionization is proportional to the H I and He II fractions, which decline with decreasing total baryon density. Since the energy of the photoejected electrons must be shared with all the baryons, the rate of energy deposition per particle by the radiation field is diminished in lower density regions. For densities $n_{\rm H} < 10^{-4}\,{\rm cm}^{-3}$, the energy deposition rate lags behind the cooling rate due to cosmic expansion. A consequence of this effect is that the temperature of the low column density systems will be sensitive to the assumed average baryon density and to the

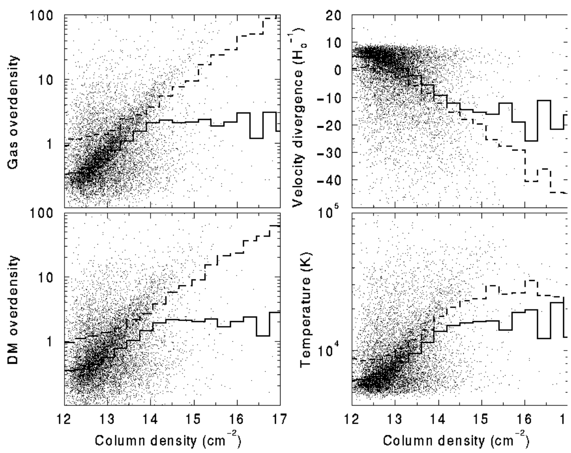

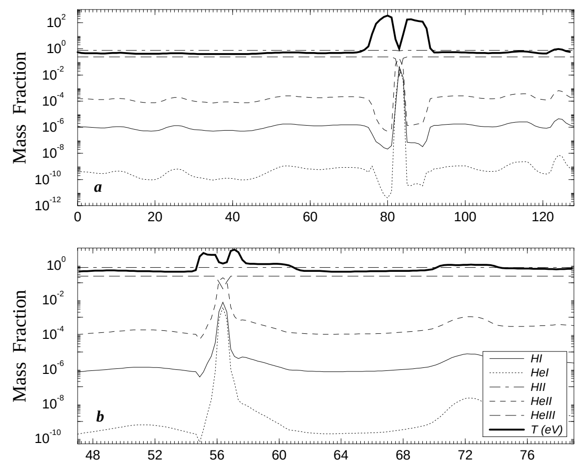

Fig. 7.— Scatter plots showing the correlations between cloud baryon and dark matter overdensities, divergence of the peculiar velocity, and temperature with H I column density, at $z = 3$. Also shown are the median (*solid line*) and mean (*dashed line*) of the distributions. Although there is substantial scatter, the internal physical properties of the absorbers correlate extremely well with the H I column density.

Fig. 8.— Line plots across a single cell at $z = 3$ through the densest structures in the (a) top and (b) subgrids. The $x-$axis is the cell number. The axis for the subgrid is renumbered to show that the subgrid resolution is four times that of the top grid. The $y-$axis is the mass fraction of each species, relative to the total baryonic mass, and the temperature is in units of eV. (Note that the two plots correspond to different lines through the box since the densest structure in the top grid is not covered by the subgrid.)

ionization history of the IGM. As the universe evolves, a greater fraction of the baryons are heated to high temperatures by compression as more massive systems continue to collapse. At the same time, the baryons in the underdense regions continue to cool through adiabatic expansion. The result, shown in Figure 9, is a progressive flattening of the temperature distribution with time.

3.2.2. Characteristic Cloud Sizes and Masses

We may use the correlations in Figure 7 to derive several key properties of the absorbers. Because of the correlation between density and column density, the neutral hydrogen fraction will be correlated with the column density as well. This relation may be used to derive the distribution of baryons within the forest as a function of column density (see the following section). A cloud with an internal density ρ_b that is optically thin at the Lyman edge and in ionization equilibrium with the metagalactic radiation field will have a neutral hydrogen density of

$$n_{\rm HI} \simeq 7\times10^{-15}\,{\rm cm}^{-3}\left(\frac{\rho_b}{\bar\rho_b}\right)^2(1+z)^6T_4^{-0.75}\Gamma_{\rm HI,-12}^{-1}, \tag{1}$$

where $\bar\rho_b$ is the cosmic mean baryon density, here taken to correspond to $\Omega_b h_{50}^2 = 0.06$. The temperature factor is due to the temperature dependence of the radiatiave recombination rate. Figure 7 shows that, in the column density range $12.5 < \log N_{\rm HI} < 14.5$, the internal cloud density varies with column density as $\rho_b/\bar\rho_b \approx N_{\rm HI,13}^{1/2}$ at $z = 3$, where $N_{\rm HI,13}$ is the H I column density in units of $10^{13}\,{\rm cm}^{-2}$.

A direct consequence of the square–root dependence of the cloud density on H I column density over the range $12.5 < \log N_{\rm HI} < 14.5$ is that the clouds in this range must all have nearly the same characteristic dimension. Taking the line–of–sight total scale length of the absorbers to be $\ell \equiv N_{\rm HI}/n_{\rm HI}$, we find from eq.(1) and $\rho_b/\bar\rho_b \approx N_{\rm HI,13}^{1/2}$ that $\ell \approx 100 - 150\,{\rm kpc}$, with a weak dependence on column density through the cloud temperature. The associated characteristic cloud baryonic masses are $M_c \equiv \rho_b(\ell)^3 \approx 0.3 - 3\times10^9\,{\rm M}_\odot$, or greater allowing for the elongation into filaments. The inferred sizes are close to the typical filament widths shown in Figure 1, and are consistent with the results of the double line–of–sight analysis performed by Charlton et al. (1997). It is also close to the scale height expected on dimensional grounds for photoionized gas in hydrostatic equilibrium within the potential well of a moderate dark matter overdensity. For a given dark matter overdensity $\rho_{\rm DM}/\bar\rho_{\rm DM}(>1)$, the equation of hydrostatic equilibrium for an isothermal gas, $c_s^2\nabla\log\rho_b = -\nabla\phi$, where c_s is the isothermal sound speed, and introducing a scaleheight r, becomes $c_s^2/r \approx (1/2)(\rho_{\rm DM}/\bar\rho_{\rm DM})H(z)^2r$, where we have expressed the gravitational potential (up to an additive constant), as $(1/4)(\rho_{\rm DM}/\bar\rho_{\rm DM})H(z)^2r^2$. We then obtain for a typical total thickness

$$\ell \approx 2r \approx 2^{3/2}\left(\frac{\rho_{\rm DM}}{\bar\rho_{\rm DM}}\right)^{-1/2}\frac{c_s}{H(z)} \approx 30 - 70\,{\rm kpc}\,, \tag{2}$$

for $\rho_{\rm DM}/\bar\rho_{\rm DM} \approx 1 - 5$. From eq.(1), and taking the overdensity in baryons to be comparable to that in the dark matter, the typical column densities of the moderately overdense systems is then

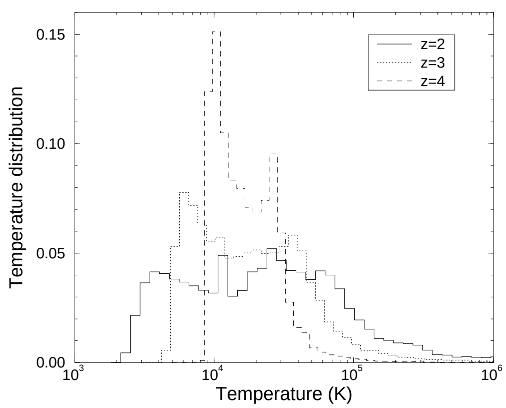

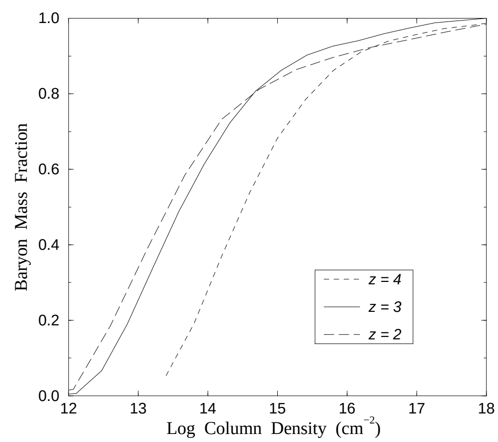

Fig. 9.— Gas temperature distribution, weighted by baryon density, at $z = 2$ (*solid line*), 3 (*dotted line*), and 4 (*dashed line*). While at $z = 4$ most of the gas is near the temperature corresponding to photoionization thermal equilibrium, the distribution flattens with time as massive regions continue to form and accrete material and the underdense regions continue to cool due to adiabatic expansion.

Fig. 10.— Cumulative distributions of the baryons below a given H I column density at $z = 2$, 3, and 4. Most of the baryons in the IGM lie within structures that give rise to discrete absorption features with column densities $12.5 < \log N_{\rm HI} < 14.5$ at $z = 3$. Fewer than 5% of the baryons remain in unresolved systems with $\log N_{\rm HI} < 12.5$ to be detected as a smoothly distributed uniform component.

$10^{13} < N_{\rm HI} < 10^{15}\,{\rm cm^{-2}}$, consistent with Figure 7. We may compare this with the minihalo model, for which the baryonic overdensities of the halo cores will reach the higher values of $200 - 1000$ due to spheroidal collapse and cooling (Meiksin 1994). The typical sizes of these systems will be a few kiloparsecs, and the corresponding column densities and baryonic masses will be $N_{\rm HI} \approx 10^{16} - 10^{17}\,{\rm cm^{-2}}$ and $M_c \approx 10^8 - 10^9\,{\rm M_\odot}$. These systems correspond to the nodes of the filaments in Figure 1, though their internal structure is likely not fully resolved in the simulation. We anticipate studying these structures in greater detail using future higher resolution simulations.

Some of the statistical properties of the Lyα forest have recently been shown to be derivable from a few basic physical assumptions. Bi & Davidsen (1997) are able to reproduce results in good agreement with the observed cloud properties over the column density range $10^{13} < N_{\rm HI} < 10^{15}\,{\rm cm^{-2}}$ starting with a lognormal distribution for the baryon density, and a suitably adjusted cloud scale length. The differences between the true distributions and a lognormal (Figures 4 and 5), though, will necessarily introduce a bias in the normalization of the column density distribution and the inferred value of the cosmological baryon density. Hui, Gnedin, & Zhang (1996) are able to obtain a very good match to the column density distribution and Doppler parameters in the simulations using a semianalytic approach based on the truncated Zeldovich approximation (Coles et al. 1993). The agreement with the fully self–consistent hydrodynamical calculations offers the promise of using semianalytic methods to infer the effect of variations in the cosmological models on the dominant statistical properties of the Lyα forest.

3.3. Ionization State of the Clouds

Recently it has become possible to place constraints on the ionization parameters of the Lyα forest systems by measuring the column densities of various ionization stages of carbon and silicon. Using the Keck HIRES, and assuming a cloud temperature determined by the balance of photoeletric heating and radiative losses, Songaila & Cowie (1996) inferred a typical ionization parameter for clouds at $z \approx 3$ with $\log N_{\rm HI} > 15$ of $U \approx 0.02$, with most clouds falling in the range $0.003 < U < 0.03$. The ionization parameter is defined to be $U = n_\gamma/n_{\rm H}$, where n_γ is the number density of hydrogen ionizing photons in the ambient radiation field, and $n_{\rm H}$ is the total number density of hydrogen atoms. The best fitting models require a large break in the UV background at the He II photoelectric edge, in keeping with the break required by our simulation to reproduce the measurements of the intergalactic He II opacity (Zhang et al. 1997). By comparing the pair of column density ratios C II:C IV and Si IV:C IV, they concluded that silicon must be enriched relative to carbon by a factor of a few to several above the solar abundance ratio, consistent with evidence for a high abundance of α–processed material found in some damped Lyα systems at high redshift (Lu et al. 1997).

The ionization parameter scaling with the cosmic mean density and the intensity of the UV ionizing background differs by a factor of Ω_b from $b_{\rm ion}$, giving $U \propto \Omega_b/b_{\rm ion} \propto (n_\gamma/b_{\rm ion})^{1/2}$. This breaks the degeneracy between the baryon density and the intensity of the radiation field in $b_{\rm ion}$

alone. Combining the normalization requirement of the mean intergalactic H I opacity, which fixes $b_{\rm ion}$, with the metal absorption line ratios, which fixes U, it is possible to constrain Ω_b and n_γ (or $\Gamma_{\rm HI,-12}$) separately. This is somewhat complicated by the spectral shape of the UV background, in particular the size of the spectral break between the H I and He II photoelectric edges. Measurements of the mean He II Lyα opacity, however, provide a stringent constraint on the size of the break (Jakobsen et al. 1994; Madau & Meiksin 1994). Based on our spectral analysis (Zhang et al. 1997), we require $b_{\rm ion} = 0.004 - 0.006$ for H I at $z = 3$, and a spectral break between the H I and He II edges corresponding to $\Gamma_{\rm HI}/\Gamma_{\rm HeII} = 250 - 400$.

We may use the simulation results to assess the values of Ω_b and n_γ by comparing the cloud properties we find in the simulation with those inferred by Songaila & Cowie (1996). The principal constraint on the low ionization parameter inferred from the observations arises from the high Si IV:C IV ratio measured. The C II:C IV and C IV:H I data alone are consistent with a higher value of $U \approx 0.2$ and 1% solar abundances; however, for this value of U, Si IV would be undetectable (Bergeron & Stasińska 1986). Of 18 systems in the column density range $15 < \log N_{\rm HI} < 17$ identified by Songaila & Cowie in two lines-of-sight, almost all (17) show C IV absorption, half (9) show Si IV absorption, and a third (6) have Si IV:C IV> 0.1. It is the high incidence of this last ratio we must explain.

Haardt & Madau (1997) have computed the UV background produced by QSO sources with an intrinsic spectral index of $\alpha_Q = 1.8$ and 2. (For the simulation, we used their earlier spectra based on $\alpha_Q = 1.5$.) These spectra are based on the steep indices measured by Zheng et al. (1996) using *HST* data. We compare our results assuming the new spectra. At $z = 3 - 3.5$, the spectra give $\Gamma_{\rm HI}/\Gamma_{\rm HeII} \approx 210 - 220$ for $\alpha_Q = 1.8$, with $\Gamma_{\rm HI,-12} \approx 0.6 - 0.8$, while $\Gamma_{\rm HI}/\Gamma_{\rm HeII} \approx 330 - 340$ and $\Gamma_{\rm HI} \approx 0.5 - 0.7$ for $\alpha_Q = 2$. The density of H I ionizing photons is $n_\gamma \approx 0.5 - 1 \times 10^{-5}\,{\rm cm}^{-3}$ for both cases. An ionization parameter of $U = 0.02$ then requires an internal cloud total hydrogen density of $n_{\rm H} \approx 2.5 - 5 \times 10^{-4}\,{\rm cm}^{-3}$, corresponding to a baryonic overdensity of $\rho_b/\bar\rho_b \approx 25 - 65$. We find in the simulation at $z = 3$ that for the systems with $15 < \log N_{\rm HI} < 17$, the fractions of systems with $\rho/\bar\rho_b > 25$, 50, and 100, are 30%, 20% and 5%, respectively. Alternatively, the value of the mean cosmic baryon density could be increased. Combining with the limit above on $b_{\rm ion}$ from the H I spectral analysis, we find that we may obtain a comparable number of dense systems to that observed, but only if (1) there is a large break in the UV background at the He II photoelectric edge of $\Gamma_{\rm HI}/\Gamma_{\rm HeII} \approx 250 - 400$, (2) the abundance ratio of Si to C is increased by a factor of ~ 3 above solar (both in agreement with the findings of Songaila & Cowie), and (3) the photoionization rate of H I is $\Gamma_{\rm HI,-12} \lesssim 1$. Our best estimates for the required cosmological mean baryon density and H I photoionization rate at $z \approx 3 - 3.5$ are $0.03 \lesssim \Omega_b \lesssim 0.08$ ($h_{50} = 1$) and $0.3 \lesssim \Gamma_{\rm HI,-12} \lesssim 1$, respectively. The constraints on the UV photoionizing background are in excellent agreement with the field produced by QSOs with a steep intrinsic spectral index of $\alpha_Q \lesssim 2$. We will make a more complete comparison elsewhere.

Rauch, Haehnelt, & Steinmetz (1996) recently performed an analysis of the expected metal ion ratios for a simulation designed to study galaxy formation, finding good agreement with the

observed metal ratios, provided the Si to C ratio was higher than solar. Since their simulation was deliberately chosen to include several protogalactic clumps, it is unclear how representative the absorber properties they find are of the cosmological distribution. For example, they find $\log N_{\rm HI} = 14$ systems to be associated with a baryonic overdensity of 10–20 at $z = 3$ (their Figure 6), a factor of 3–4 higher than we obtain. This would result in a lower ionization parameter by the same factor. A simulation closer to ours is that of Hellsten et al. (1997). They claim to find a reasonable match to the Songaila & Cowie data after increasing the break at the He II photoelectric edge a factor of 10 over that of the Haardt & Madau spectrum, and assuming a high Si to C ratio.

3.4. The Baryonic Mass in the Lyα Forest

The contribution of the baryons in the Lyα forest to the closure density is given by,

$$\Omega_{\rm Ly\alpha} = \frac{1.4 m_{\rm H}}{\rho_{\rm crit}} \frac{H_0}{c} \int dN_{\rm HI} \frac{N_{\rm HI}}{f_{\rm HI}} \frac{\partial^2 N}{\partial N_{\rm HI} \partial z} (1+z)^{5/2}, \tag{3}$$

where $f_{\rm HI} \equiv n_{\rm HI}/n_{\rm H}$ is the mean fraction of neutral hydrogen in a cloud of a given column density. Using eq. (1) and the relation found between cloud overdensity and H I column density at $z = 3$ above, $\rho_b/\bar{\rho}_b \approx N_{\rm HI,13}^{1/2}$, we obtain $f_{\rm HI} \approx 4 \times 10^{-6} N_{\rm HI,13}^{1/2} T_4^{-0.75}$ for clouds with $12.5 < \log N_{\rm HI} < 14.5$. The H I column density distribution varies nearly like $N_{\rm HI}^{-1.5}$. We then obtain

$$\Omega_{\rm Ly\alpha} \propto \log \left(\frac{N_{\rm HI,max}}{N_{\rm HI,min}} \right). \tag{4}$$

Most of the baryons lie in the column density range $12.5 < \log N_{\rm HI} < 14.5$, distributed equally per decade in column density. A more quantitative comparison with the distribution of the baryons may be made by allowing for the temperature dependence of the clouds on column density, as given in Figure 7. Taking $T_4 \simeq 0.8\, N_{\rm HI,13}^{1/4}$, so that $f_{\rm HI} \approx 5 \times 10^{-6} N_{\rm HI}^{5/16}$, and using the column density distribution fit over the range $2 \times 10^{12} < N_{\rm HI} < 10^{14}\ {\rm cm}^{-2}$ of $\partial^2 N/\partial N_{\rm HI,13} \partial z \approx 6 N_{\rm HI,13}^{-1.4} (1+z)^{2.5}$ (Zhang et al. 1997), in close agreement with Hu et al. (1995), we obtain

$$\Omega_{\rm Ly\alpha} \simeq 3.6 \times 10^{-6} N_{\rm HI,max}^{0.29} \left[1 - \left(\frac{N_{\rm HI,min}}{N_{\rm HI,max}} \right)^{0.29} \right]. \tag{5}$$

The contribution from clouds in the range $12.5 < \log N_{\rm HI} < 14$ is then $\Omega_{\rm Ly\alpha} \approx 0.03$, or 50% of the baryons in the simulation. The direct computation shown in Figure 10 yields a comparable value for the baryonic mass in clouds with column densities in this range. Because we do not reproduce the column density distribution for $\log N_{\rm HI} \gtrsim 16.5$ (Zhang et al. 1997), the distribution of the baryons among the high column density systems is uncertain. In particular, a larger box simulation may show a greater concentration of baryons in the highest column density systems, especially the Damped Lyα Absorbers. Only a tiny fraction of the baryons, less than 5%, remains in a diffuse component unresolved as low column density discrete systems. Even this small component would

possibly be shown to be discrete in a higher resolution simulation. Virtually the entire intergalactic medium has fragmented.

Meiksin & Madau (1993) and Press & Rybicki (1993) had previously suggested that most of the baryons may reside in the Lyα forest, provided the clouds were large, with sizes of ~ 100 kpc. Meiksin & Madau argued that this would be a natural means of reconciling the predictions of Big Bang nucleosynthesis for the density of the IGM and Gunn–Peterson constraints on the H I density of a smooth diffuse IGM component with a metagalactic UV radiation field dominated by QSO sources. In their constant expansion rate model, for which the clouds have a size of $100 - 200$ kpc at $z = 2.5$, Meiksin & Madau estimated $\Omega_{\mathrm{Ly}\alpha} \simeq 0.07$, in very good agreement with the results presented here.

3.5. Origin of Spectral Features

In Figure 11, we show the relation between the absorption features and the density contrasts responsible for them. Two effects are particularly noteworthy. The overdensities are plotted on a velocity scale attached to the comoving frame, while the spectra include the effects of the peculiar velocity field of the baryons on the spectral features. Although each spectral absorption feature may be identified with an upward baryon fluctuation relative to its local background, the features do not always line up in velocity space. The density enhancements that give rise to the Lyα absorbers have systemic peculiar velocities of as much as a few hundred kilometers per second.

The second effect is that many discrete absorption features are associated with fluctuations that are *underdense* relative to the cosmic average density, both in the baryons and the dark matter, as shown in Figure 7. These features tend to be those that are optically thin at line center, for which $N_{\mathrm{HI}} < 10^{13}\,\mathrm{cm}^{-2}$. Because the dark matter density associated with the features tends to be below the cosmic average, these structures appear not to be gravitationally bound. Yet, as shown in Figures 7 and 11, no pronounced separation between the baryons and the dark matter is found. In the following section, we investigate these apparently anomalous structures found for the lowest column density systems.

In Figure 12 we show a scatter plot of the ratio of the Doppler parameter of the H I features to the value expected due to thermal broadening alone, $b_{\mathrm{th}} = (2kT/m_{\mathrm{H}})^{1/2}$. A substantial contribution to the line–broadening derives from nonthermal motion within the clouds. This may be due to internal structure within the clouds that is unresolved in the H I absorption feature due to the finite velocity width of the lines. Hu et al. (1995) argue for subcomponents based on the spread in b–parameters. Cowie et al. (1995) similarly argue for subcomponents based on the number of C IV features found in systems with $\log N_{\mathrm{HI}} > 14.5$ (see also Songaila & Cowie 1996). The simulations typically find subcomponents in C IV as well, assuming a uniform enrichment of carbon (Haehnelt et al. 1996; Zhang et al. 1997).

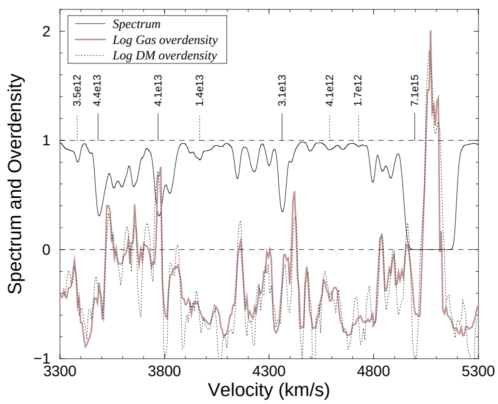

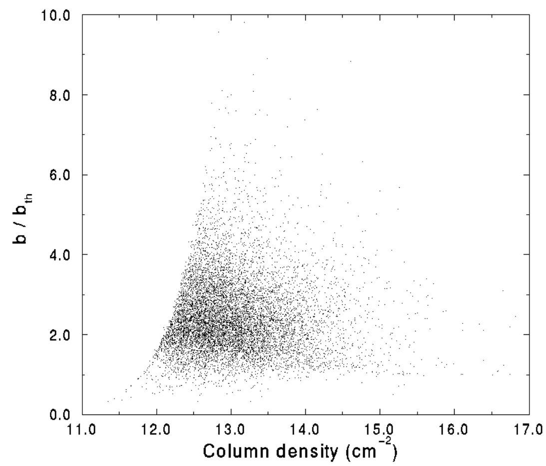

Fig. 11.— A sample of the absorption spectrum along a line–of–sight through the box at $z = 3$, as a function of velocity in the rest frame of the box. Also shown are the baryonic and dark matter overdensities that give rise to the absorption features. The densities are plotted according to their positions in the comoving frame, while the absorption features include the effects of the gas peculiar velocity. Systemic offsets of up to $100\,\mathrm{km\,s^{-1}}$ occur between a density feature in the gas and the corresponding spectral feature. The baryon fluctuations in general closely follow the dark matter fluctuations, even when both fluctuations are underdense relative to the cosmic mean. These regions give rise to optically thin absorption features.

Fig. 12.— A scatter plot of the ratio of Doppler parameter b to the thermal Doppler parameter $b_{\rm th}$ for the temperature of the gas cloud, as a function of H I column density. A substantial contribution to the Doppler parameter is nonthermal, arising from bulk motions within the clouds. The cutoff along the left of the distribution is due to selecting only systems with line center opacity exceeding 0.05.

3.6. H I Opacity Distribution

In Zhang et al. (1997), we showed that it was possible to account for the mean intergalactic H I and He II Lyα absorption entirely by discrete absorption systems identified in the simulated spectra. No evidence for a significant residual opacity due to the Gunn-Peterson effect was found. We now ask if the same is true of the full opacity distribution of the spectra. In Figure 13, we show the probability distribution $P(\tau)$ for an optical depth in the range $(\tau, \tau + d\tau)$ in a given pixel in the synthetic spectra. The pixel widths are set at $0.6\,\mathrm{km\,s^{-1}}$. In the left panel, we show the evolution of the opacity distribution for both the top grid and subgrid. Both because the subgrid is centered on an underdense region and because it is a factor 64 smaller in volume, we do not expect perfect correspondence with the top grid, but the agreement between the top and subgrid results shows that we are resolving the essential structures responsible for the spectral opacity.

In the right panel, we attempt to reproduce the distribution at $z = 3$ from a discrete line model using the results found in Zhang et al. (1997) for the distribution in line center opacity τ_0 and Doppler parameter b of the Lyα forest lines identified in our synthetic spectra, as given by Voigt profile fitting. There we found that for $\tau_0 > 0.05$, the best power law fit to the line center opacity distribution, $dN/d\tau_0 \propto \tau_0^{-\beta}$, was given by $\beta = 1.64$. We adopt a lognormal distribution for the Doppler parameters according to Zhang et al. of $f(b) \propto \exp[-6.8 \log^2(b/26.1)]$. (We find that our results are not substantially altered by choosing the best fitting gaussian distribution instead.) Because the number of lines diverges at the low end for a perfect power law, it is necessary to impose a lower cutoff to the distribution. The resulting spectral opacity distribution $P(\tau)$ for small values ($\tau \ll 0.1$), is affected by the choice of a minimum τ_0. Decreasing the minimum forces the distribution $\tau P(\tau)$ to turn down at increasingly larger values of τ. The reason for this behavior is that as the number of clouds is increased, the occurrence of a low opacity excursion in a given pixel becomes increasingly improbable: the forest tends to blanket the spectrum everywhere. The extension of the distribution in Figure 13 to very low values (we still find a signal for $\tau < 0.001$), shows that the limit of a continuum in spectral coverage is actually not reached. The distribution in τ_0 does in fact cut off.

Using the above distributions, we perform Monte Carlo realizations of the spectra in order to determine if the spectral opacity distribution may be accounted for entirely by a line model. We adjust the lower cutoff for two power-law models, $\beta = 1.64$ and $\beta = 1.5$, in order to obtain a good match to $P(\tau)$. We find each reproduces different regions in τ well, but neither is completely satisfactory. We next perform realizations drawing τ_0 from the actual line center opacity distribution we obtain from the simulated spectra. Since the distribution becomes incomplete for low values, we use the measured distribution only for $\tau_0 > 0.1$. We then extrapolate the distribution to lower values using a power law. We are now able to reproduce the spectral opacity distribution $P(\tau)$ to high precision, as shown by the thick gray curve in Figure 13. The fit shown is for $\beta = 1.55$ and $\tau_0 > 5 \times 10^{-4}$ for the low τ_0 extension. For the adopted mean Doppler parameter, the lower cutoff corresponds to a neutral H I column density of $N_{\mathrm{HI}} = 1.7 \times 10^{10}\,\mathrm{cm^{-2}}$. Because a sharp cutoff is artificial, this value should only be taken as an indication of the magnitude in column density

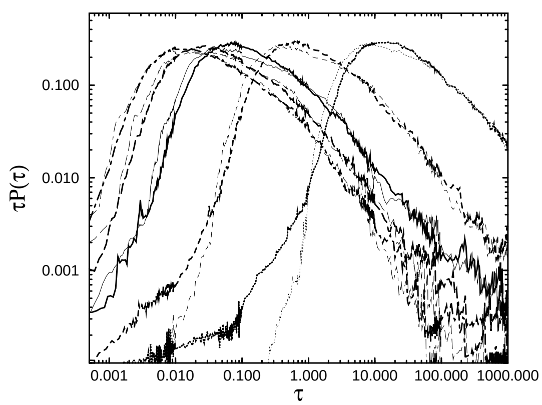

Fig. 13.— (a) The distribution of H I opacity in the spectra at $z = 5$ (*dotted*), $z = 4$ (*short–dashed*), $z = 3$ (*solid*), $z = 2.4$ (*long–dashed*), and $z = 2$ (*dot–dashed*). The heavy lines are for the top grid and the light lines for the subgrid. The agreement between the top and subgrids shows that the simulation has converged. The subgrid opacity is somewhat lower because the subgrid was placed on an underdense region. (b) The opacity distribution at $z = 3$ from the simulation (*solid*), and for two line models with power law line center opacity distributions $dN/d\tau_0 \propto \tau_0^{-\beta}$, with the indicated values of β. The thick gray line shows the distribution from a line model using the measured τ_0 distribution for $\tau_0 > 0.1$, and smoothly extended to lower values using a power law with $\beta = 1.55$. The opacity distribution is well reproduced by a line model. No significant continuous Gunn–Peterson component is allowed.

below which relatively few systems form. The deviations at the extremities in the distribution we believe are due to sampling error and possible curvature in the τ_0 distribution at low values. We thus conclude that the full spectral opacity distribution $P(\tau)$ may be accounted for entirely by line blanketing due to discrete absorption systems with Voigt line profiles. If a smoothly distributed, homogeneously expanding H I component were present, the spectral opacity distribution would cut off abruptly at the opacity corresponding to its H I density. Figure 13 shows no such component exists.

We may compare the distribution at $z = 2.4$ with that of Croft et al. (1997) at $z = 2.33$ (their Figure 11), based on a TreeSPH calculation. While the two distributions agree in shape for $\tau > 0.05$, we find a tail at lower values that is absent in the Croft et al. distribution, which cuts off at $\tau < 0.004$. The tail is a signature of the low opacity regions in the spectrum that result from the ubiquitous clumping of the gas. A comparison between Figure 11 and Figure 4 of Croft et al. shows that we obtain substantially more structure in the transmitted flux and underlying gas distribution than in the TreeSPH simulation. In §3.2.2 above, we showed that the characteristic cloud sizes and masses were 100 kpc and $M_c \approx 10^9\,\mathrm{M}_\odot$. The mass of the gas particles in the simulation of Croft et al. is $1.5 \times 10^8\,\mathrm{M}_\odot$, not much less than the cloud masses. We believe that the reason the low opacity structure is absent in their simulation is that they are under-resolving the clumping of the gas. Under–resolving the clumping will contribute to the higher opacity values they obtain compared to our results (Zhang et al. 1997).

4. Cosmic Minivoids

In this section, we discuss in greater detail the absorption and evolution of discrete systems in the underdense regions. We believe it illuminating to distinguish these systems from the remainder of the Lyα forest for several reasons: 1. We find considerable structure in the underdense regions, more than can be accounted for by the Jeans instability. 2. The systems are diffuse, and hence behave similarly to a smooth IGM component in their averaged absorption properties, but not identically to one. 3. The recent and anticipated space–based detections of intergalactic He II essentially are probes of the fine structure of the minivoids. Since the current and near–term detectors are not generally capable of resolving individual He II Lyα absorption systems, a discussion of the underlying physical properties of the clouds in the underdense regions is crucial for interpreting future He II measurements in the context of CDM and reionization models. Critical to the discussion is establishing convergence to the correct amount of He II absorption. Without adequate resolution of the structures giving rise to the absorption, the amount of absorption will be over–estimated.

4.1. Physical Structure

The low physical densities associated with the low column density H I systems was previously demonstrated in Figures 1 and 2. In Figure 11, we show a direct comparison between the H I absorption and the associated underlying baryon and dark matter density fluctuations at $z = 3$. For H I column densities below about $10^{13}\,\mathrm{cm}^{-2}$, lines that are optically thin in Lyα at line center, the typical baryonic and dark matter densities of the systems are below the cosmic average. The low densities present a difficulty for accounting for their origin, since such low density systems appear not to have formed from a Jeans instability. The baryonic proper Jeans length in a medium of mixed dark matter and baryons is $\lambda_J = 2\pi(2/3)^{1/2}c_s/H(z)$, where c_s is the sound speed of the baryons associated with a linear perturbation and $H(z)$ is the Hubble constant at redshift z (e.g., Bond & Szalay 1983). For an isothermal perturbation, $\lambda_J \simeq 1\,\mathrm{Mpc}\,h_{50}^{-1}T_4^{1/2}(1+z)^{-3/2}$, or about 150 kpc at $z = 3$. This gives a minimal column density due to Jeans instability of $\log N_{\mathrm{HI}} \simeq 13$ at $z = 3$. The corresponding baryonic Jeans mass is $M_J \equiv \langle\rho_b\rangle\lambda_J^3 \simeq 4\times10^9\,\mathrm{M}_\odot\,(\Omega_b h_{50}^2/0.06)h_{50}^{-3}T_4^{3/2}(1+z)^{-3/2}$, or $\sim 4\times10^8\,\mathrm{M}_\odot$ at $z = 3$. The power–spectrum of the density fluctuations for short wavelength modes, $\lambda \ll \lambda_J$, will be suppressed by the factor $(\lambda/\lambda_J)^2$. Thus, one might reasonably expect a downturn in the H I column density distribution below $\sim 10^{13}\,\mathrm{cm}^{-2}$.

This line of argument was pursued by Reisenegger & Miralda-Escudé (1995), who concluded that the diffuse optically thin systems would merge into a 'fluctuating Gunn-Peterson effect.' No indication of a suppression in the column density distribution at $10^{13}\,\mathrm{cm}^{-2}$ is apparent in Figure 14 (reproduced from Zhang et al. 1997): the power–law column density distribution persists to column densities well into the optically thin regime, with a slope consistent with measurements of the Lyα forest by the Keck HIRES (Hu et al. 1995). Figure 7 shows that the low column density absorbers are associated with structures that are underdense both in the baryons and the dark matter distributions. If they formed from Jeans unstable fluctuations, the opposite would be true. Thus *we find discrete absorption systems that appear not to have formed from a Jeans instability.* It is crucial to resolve the low column density systems for assessing the amount of He II absorption predicted by the model. We would therefore like to understand the origin of these systems to ensure that we are able to converge to the correct average intergalactic He II opacity.

A clue to the formation mechanism of the highly diffuse clouds is suggested by a comparison of the low H I column density contours in Figure 2 with the peculiar velocity divergence contours in Figure 1. The low H I column density systems tend to associate with regions of positive peculiar velocity divergence. The optically thin systems are not equilibrium structures: their density is dissipating at a rate in excess of the average cosmic expansion. In principle, low column density gas could be associated with low mass minihalos. Bond et al. (1988) demonstrated that the baryons bound to low mass minihalos prior to reionization may be reheated to temperatures too high for the minihalos to retain the gas after reionization, and the baryons will escape. While this must occur for some systems, a comparison with the dark matter overdensity for the optically thin features in Figures 7 and 11 show that these systems are generally not associated with minihalos, since the dark matter fluctuations themselves are below the cosmic average. Statistically, no substantial

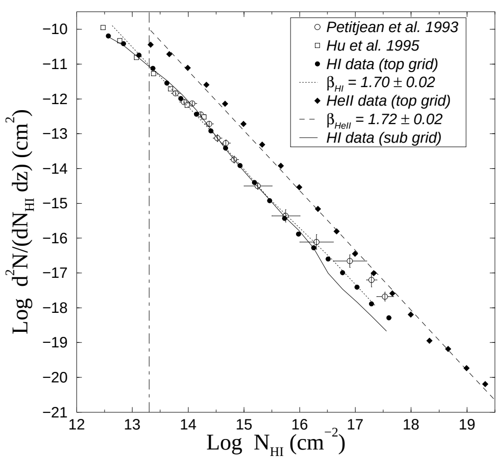

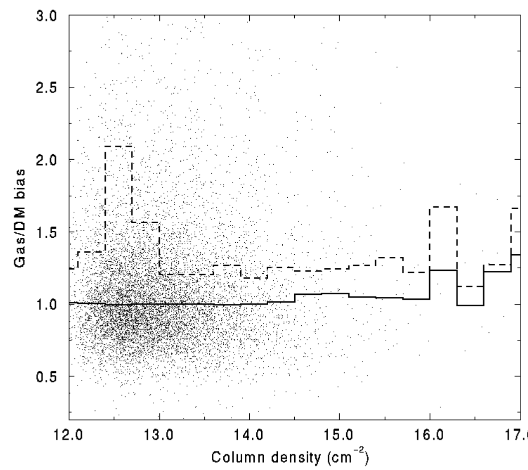

Fig. 14.— H I (filled circles) and He II (filled diamonds) column density distributions at $z = 3$. Also shown are the observed data from Petitjean et al. (1993) and Hu et al. (1995). The dotted and dashed lines are the least–squares power law fits to the entire column density ranges of H I and He II respectively. The solid line represents the H I distribution derived from data on the higher resolution subgrid. The subgrid is centered on an underdense region in the box, and so it misses the highest column density systems. The vertical dashed line indicates $N_{\rm HI} = 2 \times 10^{13}\,{\rm cm}^{-2}$, the dividing line between the optically thin and thick components.

Fig. 15.— Scatter plot of the ratio of gas to dark matter overdensities as a function of H I column density, at $z = 3$.

separation of the baryons from the dark matter is found for these low column density systems, as shown in Figure 15.

Another possibility is that the features arise from velocity caustics, regions for which a convergence in the line–of–sight velocity field compresses the absorption in redshift, hence wavelength, space (McGill 1990). This is possible even in low density regions where the flow field is divergent, since the gas may be expanding in the directions lateral to the line–of–sight. In Figure 16 we show a scatter plot of the line–of–sight velocity derivative dv_z/dz as a function of $N_{\rm HI}$, where v_z is the component of the peculiar velocity along the line–of–sight. The low column density absorbers tend to have $dv_z/dz > 0$, opposite to the criterion required for velocity caustics.

Meiksin (1997) has suggested an interpretation of these features in terms of the growth of fluctuations in an underdense background. A fluctuation that is underdense compared to the mean cosmological value but overdense relative to a large surrounding underdense region will grow as if in an open universe. After an initial period of growth relative to the diminishing local background, the relative density perturbation will 'freeze', very roughly at an epoch given by $1+z_f \approx \Omega_v^{-1} - 1$, where Ω_v is the ratio of density in the background void to the Einstein–deSitter critical density. Thus, although the physical density of the absorber diminishes with time like the density of the background void, it retains its integrity as a discrete entity as the void continues to expand.

4.2. Optically Thin H I Absorption

The resonant opacity arising from a uniform medium of H I density $\bar{n}_{\rm HI}$ in a homogeneously expanding universe is given by (Field 1959; Gunn & Peterson 1965)

$$\tau_\alpha = \left(\frac{\pi e^2}{m_e c}\right) f_\alpha \lambda_\alpha \frac{1}{H_0} \frac{\bar{n}_{\rm HI}}{(1+z)(1+2q_0 z)^{1/2}}, \tag{6}$$

where f_α is the upward oscillator strength for Lyα , and λ_α is the Lyα rest wavelength. (A zero cosmological constant is assumed, so that $q_0 = \Omega_0/2$.) What is the effect on the opacity of aggregating the gas into discrete clouds? Provided that the only clouds considered are those that are individually optically thin, the expression for the opacity is unchanged if $\bar{n}_{\rm HI}$ is identified with the spatially averaged density of the neutral hydrogen. This is distinct from the average internal neutral density $n^c_{\rm HI}$ of the individual clouds when their volume filling factor f_c is less than unity (e.g., Meiksin 1997). The two are related by $\bar{n}_{\rm HI} = f_c \bar{n}^c_{\rm HI}$. Eq. (6) shows that the optically thin component of the Lyα forest behaves similarly, but not identically, to a diffuse homogeneous gas component. While the opacity in both cases is in direct proportion to the spatially averaged neutral hydrogen density, and so inversely proportional to the metagalactic UV radiation field, the opacities need not evolve in the same way, both because the cloud internal density need not evolve like the cosmological expansion, and because of any evolution of the filling factor.

The presence of the volume filling factor precludes inverting eq. (6) to solve for the spatially averaged total hydrogen density of the optically thin systems. If the internal density of the clouds,

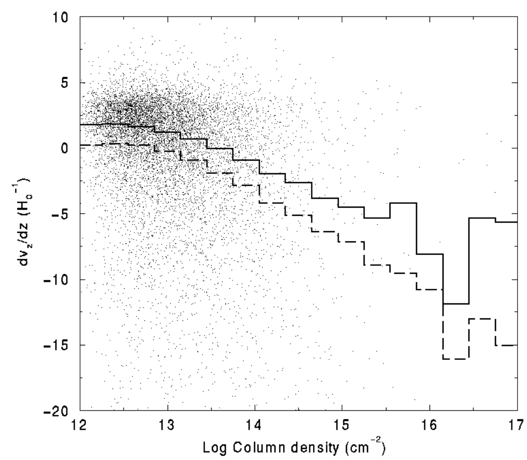

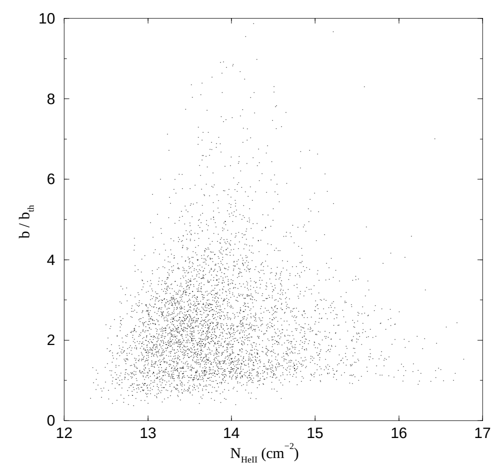

Fig. 16.— Scatter plot of the line–of–sight peculiar velocity divergence as a function of H I column density, at $z = 3$.

Fig. 17.— A scatter plot of the ratio of He II Doppler parameter b to the thermal Doppler parameter $b_{\rm th}$ for the temperature of the gas cloud, as a function of He II column density. A substantial contribution to the Doppler parameter is nonthermal, arising from bulk motions within the clouds. The cutoff along the left of the distribution is due to selecting only systems with line center opacity exceeding 0.05.

however, is less than the cosmic mean density, then we may derive a lower limit to the cosmic mean density given a measurement of τ_α from the optically thin systems. (Since the result that the optically thin clouds are underdense is obtained from the simulations, this is actually a consistency check on the simulation results rather than an independent determination of Ω_b.) The sample of Hu et al. (1995) may be used for making such a determination. Counting only lines with line center Lyα opacity less than 0.5, to be conservative, and weighting each line inversely by the estimated incompleteness factor for its H I column density according to their Table 3, we obtain $\tau_\alpha \approx 0.07$. Combining with eq. (1), and requiring $\rho_b^c < \bar{\rho}_b$, where ρ_b^c is the internal cloud baryon density and $\bar{\rho}_b$ is the average cosmological baryon density, we obtain $\Omega_b > 0.02h_{50}^{-3/2}$, consistent with the value $\Omega_b = 0.06$ adopted in the simulation.

4.3. Intergalactic He II Absorption

A consequence of the low nonequilibrium temperature of the gas inside the minivoids is that the temperature of the systems giving rise to the low column density absorbers ($N_{\rm HI} < 10^{13}\,{\rm cm}^{-2}$), will be history–dependent; i.e., it will depend on the photoionization history of the baryons and their expansion history, which in turn depends on the local density inhomogeneities. The temperature will depend on the actual density of the gas as well. In this case, the Doppler parameters of the low column density lines are no longer independent of $b_{\rm ion}$. This is especially important for determining the amount of He II absorption, since it sets the widths of the absorption features, hence the total amount of absorption once the lines begin to enter the saturated part of the curve–of–growth. In practice, the effect is reduced by the presence of nonthermal broadening of the lines due to bulk motions. In Figure 17, we show a scatter plot of the ratio of the Doppler parameters to the thermal Doppler parameter at the cloud temperature, as a function of $N_{\rm HeII}$. A large contribution to the widths of the lines derives from bulk motion within the clouds.

In Figure 18 we show a representative He II spectrum at $z = 3$. As for the H I , the spectral features tend to be associated with discrete baryonic density fluctuations. Because of the higher density of He II compared to H I , however, these features are largely associated with fluctuations in the underdense regions: He II absorption provides a probe of the cosmic minivoids. Because of the sensitivity of the void temperature and baryonic density structure to the rate of expansion within the voids and the ionization history, the He II opacity may provide a useful means of discriminating between rival cosmological models and reionization scenarios. To do so, however, it is crucial that the structure within the voids be resolved sufficiently to ensure convergence to the correct total He II opacity.

We show in Figure 19 the evolution of the distribution function $P(\tau)$ of the He II spectral opacity from the top grid calculation for $2 < z < 5$. At $z = 2.4$, we also show the opacity distribution from the subgrid calculation. The subgrid and top grid distributions agree well, showing that we have resolved the features that produce the He II opacity. The opacity is somewhat lower in the subgrid because we have centered it on a low density region. We found in Zhang et al. (1997) that

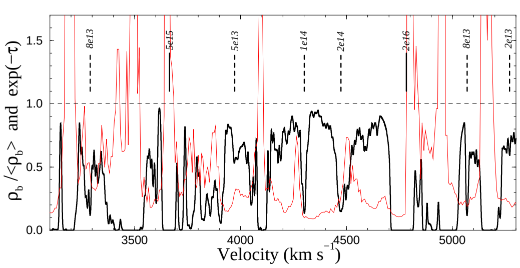

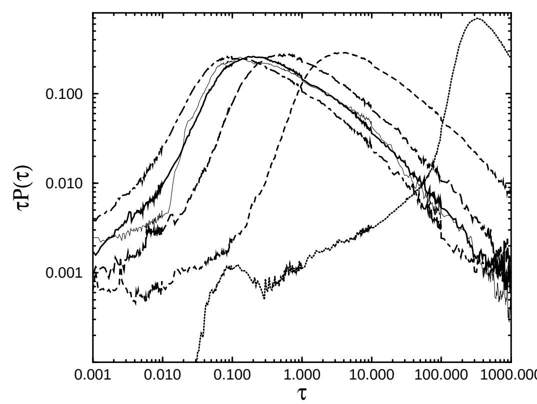

Fig. 18.— A sample of the He II absorption spectrum along a line–of–sight through the box at $z = 3$. Also shown (*light line*) is the baryonic overdensity that gives rise to the absorption features. Most of the discrete He II systems arise from density fluctuations in underdense regions.

Fig. 19.— The distribution of He II opacity in the spectra at $z = 5$ (*dotted*), $z = 4$ (*short–dashed*), $z = 3$ (*long–dashed*), $z = 2.4$, both for the top grid (*heavy solid*), and the subgrid (*light solid*), and $z = 2$ (*dot–dashed*). The agreement between the top and subgrid distributions shows that the simulation is resolving the essential features that determine the mean intergalactic He II opacity.

matching to the intergalactic He II opacity measurements required a break in the UV background intensity between the H I and He II photoelectric edges by a factor of 100–150. This is consistent with the break required to match the amount of Si and C absorption measured in the Lyα forest by Songaila & Cowie (1996) (§3.3).

5. Summary

We summarize our main results.

1. The structures giving rise to the Lyα forest cloud population are characterized by a range of morphologies, with different structures associated with different ranges in H I column density. The high column density absorbers ($N_{\rm HI} > 10^{15}\,{\rm cm}^{-2}$ and $N_{\rm HeII} > 10^{17}\,{\rm cm}^{-2}$) correspond to the highly overdense structures ($\rho_b/\overline{\rho}_b > 10$) residing mostly along and at the intersections of filaments. The medium column density absorbers ($10^{13} \lesssim N_{\rm HI} \lesssim 10^{14}\,{\rm cm}^{-2}$ and $10^{15} \lesssim N_{\rm HeII} \lesssim 10^{16}\,{\rm cm}^{-2}$) correspond to the modestly overdense filaments ($1 < \rho_b/\overline{\rho}_b < 5$). The column density can be coherent over the scale of a few megaparsecs at this level. The lowest column density absorbers ($N_{\rm HI} \sim 10^{12}\,{\rm cm}^{-2}$ and $N_{\rm HeII} \sim 10^{14}\,{\rm cm}^{-2}$) are associated with underdense structures ($\rho_b/\overline{\rho}_b < 1$) and are located in the void regions between the filamentary structures. They are typically a few hundred kiloparsecs across. The associated flow pattern of the structures is one of outflow from the voids, compression into sheets at the boundaries of the voids, and a resulting flow along the sheets toward their intersections, where the densest structures form.

2. The principal density structures are in place by $z = 5$, with only moderate evolution in the baryon overdensity at later times. By contrast, the post–reionization temperature is initially narrowly peaked at the photoionization value, and flattens toward higher and lower values with time as dense massive structures continue to collapse and the voids continue to cool by expansion.

3. The baryon overdensity, dark matter overdensity, baryon temperature, and divergence of the baryon peculiar velocity field all show strong correlations with the H I column density of the associated absorption features. For $12.5 < \log N_{\rm HI} < 14.5$ at $z = 3$, we obtain $\rho_b/\langle\rho_b\rangle \approx N_{\rm HI,13}^{1/2}$, $T_4 \approx 0.8 N_{\rm HI,13}^{1/4}$, and $f_{\rm HI} \approx 5 \times 10^{-6} N_{\rm HI,13}^{5/16}$, where $N_{\rm HI,13}$ is the H I column density in units of $10^{13}\,{\rm cm}^{-2}$, and T_4 is the baryon temperature in units of 10^4 K. The baryonic density scaling requires that all clouds in this column density range have the same characteristic size of $N_{\rm HI}/n_{\rm HI} = 100-150$ kpc. The associated cloud mass is $0.3 - 3 \times 10^9\,{\rm M}_\odot$.

4. The simulation is able to reproduce the statistics of the carbon and silicon measurements of the Lyα forest at $z \sim 3$ of Songaila & Cowie (1996) and the intergalactic He II opacity measurements, provided the UV background has a break of $\Gamma_{\rm HI}/\Gamma_{\rm HeII} \approx 250 - 400$ and the Si to C abundance ratio is a few times the solar value. Combining with the limits on $b_{\rm ion}$ from our spectral analysis (Zhang et al. 1997), we obtain for best estimates of the cosmic mean baryon density and UV background $0.03 \lesssim \Omega_b \lesssim 0.08$ ($h_{50} = 1$), and $0.3 \lesssim \Gamma_{\rm HI,-12} \lesssim 1$ at $z \approx 3 - 3.5$. The constraints on the radiation

field are consistent with a UV background dominated by QSO sources with a spectral index of $\alpha_Q \approx 1.8 - 2$, in agreement with the indices measured by Zheng et al. (1996). These values are sensitive to the assumed normalization and shape of the primordial power spectrum.

5. We find that half of the baryons in the simulation are contained within clouds with H I column densities in the range $12.5 < \log N_{\rm HI} < 14$ at $z = 3$, and that fewer than 5% reside in systems that have not been identified with discrete absorption lines in the synthesized spectra.

6. The structures giving rise to the absorption systems have systemic peculiar velocities as high as $100\,{\rm km\,s^{-1}}$ and internal motions that give substantial contributions to the Doppler widths of the absorption lines.

7. The H I opacity distribution of the synthesized spectra may be fully accounted for by a distribution of discrete absorption lines. No significant uniform Gunn–Peterson component is allowed.

8. A large population of optically thin absorption lines is associated with underdense modulations in minivoids, low density regions a few megaparsecs across. Most of the intergalactic He II opacity is derived from absorption within the minivoids. The dark matter fluctuations associated with this absorber population are underdense, and the peculiar velocity field of the baryons is divergent, suggesting that the systems did not originate through a Jeans instability. They appear to have grown from small scale primordial underdense fluctuations within the larger minivoid. If the optically thin absorbers measured in QSO spectra are associated with underdense regions, we derive a lower bound on the cosmic baryon density of $\Omega_b h_{50}^{3/2} > 0.02$.

We are pleased to thank Ed Bertschinger, Piero Madau, David Weinberg, and Martin White for useful conversations, and Francesco Haardt for providing us with QSO dominated UV background spectra. We would also like to thank John Shalf (NCSA), for his 3D visualizations in the accompanying video tape and in Plate 1. This work is supported in part by the NSF under the auspices of the Grand Challenge Cosmology Consortium (GC^3). The computations were performed on the Convex C3880 and the SGI Power Challenge at the National Center for Supercomputing Applications, and the Cray C90 at the Pittsburgh Supercomputing Center under grant AST950004P. A.M. thanks the William Gaertner Fund at the University of Chicago for support.

REFERENCES

Abel, T., Anninos, P., Zhang, Y., & Norman, M. L. 1997, New Astronomy, in press

Anninos, P., Norman, M. L., & Clarke, D. A. 1994, ApJ, 436, 11

Anninos, P., Zhang, Y., Abel, T., & Norman, M. L. 1997, New Astronomy, in press

Arons, J. 1972, ApJ, 172, 553

Bardeen, J. M., Bond, J. R., Kaiser, N., & Szalay, A. S. 1986, ApJ, 304, 15

Bertschinger, E. 1995, astro-ph/9506070

Bergeron, J., & Stasińska, G. 1986, A&A, 169, 1

Bi, H., & Davidsen, A. F. 1997, ApJ, in press

Bond, J. R., Kofman, L., & Pogosyan, D. 1996, Nature, 380, 603

Bond, J R., & Myers, S. T. 1996, ApJS, 103, 63

Bond, J. R., & Szalay, A. S. 1983, ApJ, 274, 443

Bond, J. R., Szalay, A.S. & Silk, J. 1988, ApJ, 324, 627

Bryan, G. L., Cen, R., Norman, M. L., Ostriker, J. P., & Stone, J. M. 1994, ApJ, 428, 405

Cen, R., Miralda-Escudé,J., Ostriker, J. P., & Rauch, M. 1994, ApJ, 437, L9

Charlton, J., Anninos, P., Zhang, Y., & Norman, M. L. 1997, ApJ, in press (astro-ph/9601152)

Charlton, J. C., Salpeter, E. E., & Hogan, C. J. 1993, ApJ, 402, 493

Coles, P., & Jones, B. 1991, MNRAS, 248, 1

Coles, P., Melott, A. L., & Shandarin, S. F. 1993, MNRAS, 260, 765

Colombi, S. 1994, ApJ, 435, 536

Copi, C. J., Schramm, D. N., & Turner, M. S. 1995, Science, 267, 192

Cowie, L. L., Songaila, A., Kim, T. S., & Hu, E. M. 1995, AJ, 109, 1522

Croft, R. A. C., Weinberg, D. H., Katz, N., & Hernquist, L. 1996, ApJ, in press (astro-ph/9611053)

Davé, R., Hernquist, L., Weinberg, D. H., & Katz, N. 1997, ApJ, 477, 21

Davidsen, A., Kriss, G. A., & Zheng, W. 1996, Nature, 380, 47

Field, G. 1959, ApJ, 129, 536

Giroux, M. L., Fardal, M. A., & Shull, J. M. 1995, ApJ, 451, 477

Gunn, J. E., & Peterson, B. A. 1965, ApJ, 142, 1633

Haardt, F. & Madau, P. 1996, ApJ, 461, 20

——— 1997, ApJ, in preparation

Haehnelt, M. G., Steinmetz, M., & Rauch, M. 1996, ApJ, 465, L95

Hellsten, U., Davé, R., Hernquist, L., Weinberg, D. H., & Katz, N. 1997, ApJ, submitted (astro-ph/9701043)

Hernquist, L., Katz, N., Weinberg, D., & Miralda-Escudé, J. 1996, ApJ, 457, L51

Hogan, C. J., Anderson, S. F., & Rugers, M. H. 1997, AJ, 113, 1495

Hu, E. M., Kim, T. S., Cowie, L. L., Songaila, A., & Rauch, M. 1995, AJ, 110, 1526

Hui, L., Gnedin, N. Y., & Zhang, Y. 1996, ApJ, submitted (astro-ph/9608157)

Ikeuchi, S. 1986, Ap&SS, 118, 509

Ikeuchi, S., Murakami, I., & Rees, M. J. 1988, MNRAS, 236, 21P

Ikeuchi, S., & Norman, C. A. 1987, ApJ, 312, 485

Ikeuchi, S., & Ostriker, J.P. 1986, ApJ, 301, 522

Jakobsen, P., Boksenberg, A., Deharveng, J. M., Greenfield, P., Jedrzejewski, R., & Paresce, F. 1994, Nature, 370, 35

Jenkins, E. B., & Ostriker, J. P. 1991, ApJ, 376, 33

Lu, L., Sargent, W. L. W., Barlow, T. A., Churchill, C. W., & Vogt, S. S. 1997, ApJS, 107, 475

Lynds, C. R. 1971, ApJ, 164, L73

Madau, P., & Meiksin, A. 1994, ApJ, 433, L53

McGill, C. 1990, MNRAS, 242, 544

Meiksin, A. 1994, ApJ, 431, 109

Meiksin, A. 1997, in *Young Galaxies and QSO Absorption-Line Systems*, eds. S. M. Viegas, R. Gruenwald, & R. R. de Carvalho (San Francisco: ASP), p. 1

Meiksin, A., & Madau, P. 1993, ApJ, 412, 34

Miralda–Escudé, J., & Rees, M. J. 1993, MNRAS, 260, 617

Miralda–Escudé, J., Cen, R., Ostriker, J. P., & Rauch, M. 1996, ApJ, 471, 582

Murakami, I., & Ikeuchi, S. 1994, ApJ, 420, 68

Norman, M. L. 1996, Physics Today, 49, 42

Ostriker, J.P., & Ikeuchi, S. 1983, ApJ, 268, L63

Press, W. H., & Rybicki, G. B. 1993, ApJ, 418, 585

Rauch, M., Haehnelt, M. G., & Steinmetz, M. 1996, ApJ, submitted (astro-ph/9609083)

Rees, M.J. 1986, MNRAS, 218, 25

Rees, M.J. 1988, in *QSO Absorption Lines*, eds. J.C. Blades, D.A. Turnshek & C.A. Norman (Cambridge: Cambridge University Press)

Reisenegger, A., & Miralda-Escudé, J. 1995, ApJ, 449, 476

Sargent, W. L. W., Young, P. J., Boksenberg, A., & Tytler, D. 1980, ApJS, 42, 41

Songaila, A., & Cowie, L. L. 1996, AJ, 112, 335

Songaila, A., Hu, E. M., & Cowie, L. L. 1995, Nature, 375, 124

Steidel, C.C., & Sargent, W.L.W. 1987, ApJ, 313, 171

Wadsley, J. W., & Bond, J. R. 1997, in *Computational Astrophysics*, Proc. 12th Kingston Conference, eds. D. Clarke & M. West (San Francisco: ASP), in press (astro-ph/9612148)

White, S. D. M., Efstathiou, G., & Frenk, C. S. 1993, MNRAS, 262, 1023

Zhang, Y., Anninos, P., & Norman, M. L. 1995, ApJ, 453, L57

Zhang, Y., Anninos, P., Norman, M. L., & Meiksin, A. 1997, ApJ, in press (astro-ph/9609194)

Zhang, Y., Meiksin, A., Anninos, P., & Norman, M. L. 1996, astro-ph/9601130

Zheng, W., Kriss, G. A., Telfer, R. C., Grimes, J. P., & Davidsen, A. F. 1997, ApJ, 475, 469

Plate 1 – Isodensity contour surfaces of log baryon overdensity $(\rho_b/\bar{\rho}_b)$, at $z = 3$. The contour levels are $\log_{10}(\rho_b/\bar{\rho}_b) = -1$, –0.5, –0.3, 0., 0.5, and 1. The colors indicate temperature, ranging from 10^4 K (*blue*) to 10^5 K (*red*).